

Polygonal Eyewall Asymmetries during the rapid intensification of Hurricane Michael (2018)

Ting-Yu Cha¹, Michael M. Bell¹, Wen-Chau Lee^{2*}, Alexander J. DesRosiers¹

¹Department of Atmospheric Science, Colorado State University, Fort Collins, CO

²National Center for Atmospheric Research, Boulder, CO

Key Points:

- Single Doppler radar retrievals capture the structural evolution of Hurricane Michael's polygonal eyewall during rapid intensification.
- The propagation speeds of asymmetric winds and reflectivity are consistent with linear vortex Rossby wave theory.
- Coastal radar observations and the generalized velocity track display technique can help to improve tropical cyclone intensity forecasts.

*The National Center for Atmospheric Research is sponsored by the National Science Foundation.

Corresponding author: Ting-Yu Cha, tingyu@colostate.edu

13 **Abstract**

14 Polygonal eyewall asymmetries of Hurricane Michael (2018) during rapid intensification
 15 (RI) are analyzed from ground-based single Doppler radar. Here we present the first ob-
 16 servational evidence of the evolving wind field of a polygonal eyewall during RI to Cat-
 17 egory 5 intensity by deducing the axisymmetric and asymmetric winds at 5-minute in-
 18 tervals. Spectral time decomposition of the retrieved tangential wind structure shows
 19 quantitative evidence of high-order azimuthal wavenumbers with propagation speeds that
 20 are consistent with linear wave theory on a radial vorticity gradient, suggesting the pres-
 21 ence of rapidly-evolving vortex Rossby waves. Dual-Doppler winds from the airborne NOAA
 22 P-3 Hurricane Hunter provide further evidence of the three-dimensional vortex struc-
 23 ture that supports growth of asymmetries during RI. Both reflectivity and tangential wind
 24 fields show polygonal structure and propagate at similar speeds, suggesting a close cou-
 25 pling of the dynamics and the convective organization during the intensification.

26 **Plain Language Summary**

27 Understanding tropical cyclone (TC) structure and evolution are crucial for improv-
 28 ing weather forecasts. Hurricane Michael (2018) was observed by radar imagery to have
 29 an evolving polygonal eyewall with elliptical, triangular, and square shapes during rapid
 30 intensification (RI). While polygonal eyewall shapes have been seen in previous hurri-
 31 canes, the corresponding evolution of wind asymmetries has never been quantitatively
 32 deduced due to limitations from previous observations. Here we present the first obser-
 33 vational evidence of the evolving wind field of a polygonal eyewall during RI to Cate-
 34 gory 5 intensity by deducing the winds at 5-minute intervals from single-Doppler Next
 35 Generation Weather Radar (NEXRAD) observations. The results highlight the value of
 36 coastal radar observations to investigate physical mechanisms of TC intensity and struc-
 37 ture evolution, and will help to improve intensity forecasts in the future.

38 **1 Introduction**

39 Tropical cyclone (TC) internal dynamics are a primary factor impacting the storm
 40 evolution in an environment that is favorable for rapid intensification (RI) (Hendricks
 41 et al., 2010). Inner-core processes are intrinsically less predictable and more difficult to
 42 observe in detail than the larger-scale environment, which makes forecasts of intensity
 43 change particularly challenging. The U.S. coastal Next Generation Weather Radar (NEXRAD)

44 system network provides continuous surveillance capability of TCs with high temporal
45 and spatial resolution, and can collect valuable data on TC evolution. The axisymmetric and asymmetric tangential winds are able to be retrieved using the Generalized Velocity Track Display (GVTD) technique with single ground-based Doppler radar data
46 (Jou et al., 2008; Cha, 2018), providing insights on the TC dynamics and evolution (W.-
47 C. Lee & Bell, 2007; Shimada et al., 2018; Cha, 2018). Hurricane Michael (2018) was the
48 first Category 5 hurricane to make landfall in the United States since Hurricane Andrew
49 (1992) and caused extensive damage in Florida and Georgia (Beven II & Hagen, 2019).
50 Satellite and radar imagery showed evidence of an evolving polygonal eyewall as Michael
51 underwent RI during its approach to Florida. In this study, single Doppler radar winds
52 from a coastal radar are analyzed to provide the first observational evidence of the kine-
53 matic structure of a polygonal eyewall during RI to Category 5 intensity.
54

55 Polygonal eyewalls are hypothesized to be the result of asymmetric vorticity dy-
56 namics that can modulate TC structure and intensity through counter-propagating vor-
57 tex Rossby waves (VRWs) (Muramatsu, 1986; Schubert et al., 1999; Kuo et al., 1999;
58 Hendricks et al., 2012; Kuo et al., 2016). A sign reversal of the mean radial vorticity gra-
59 dient that acts as a waveguide for VRWs satisfies the Rayleigh condition for barotropic-
60 baroclinic instability (Montgomery & Shapiro, 1995), which can lead to a breakdown of
61 the potential vorticity (PV) ring and redistribution of eyewall PV and angular momen-
62 tum (Schubert et al., 1999; Bell & Montgomery, 2008) which can accelerate the mean
63 wind inside the radius of maximum wind (RMW), and promote the contraction of RMW.
64 The presence of a "ring" of mean vorticity that satisfies the Rayleigh condition can ex-
65 ist in both intensifying and weakening storms depending on intensity (Martinez et al.,
66 2017), suggesting that the vortex dynamics can be complex and VRWs may lead to in-
67 tensification (Menelaou & Yau, 2014), rapid weakening (Martinez et al., 2019) or steady-
68 state periods (Kossin & Eastin, 2001). J.-D. L. Lee and Wu (2018) hypothesized that
69 polygonal eyewalls acted as a possible RI mechanism in Typhoon Megi (2010) by enhanc-
70 ing the generation of convective bursts inside the RMW, which then affects the devel-
71 opment of the warm-core in the upper tropopause and the vertical alignment of the eye-
72 wall. They concluded that maintaining a certain pattern of polygonal eyewall structures
73 within the high inertial stability region for an extended period of time is beneficial to
74 RI.
75

76 Previous theoretical studies have often used a simplified barotropic nondivergent
 77 model framework to investigate the dynamical processes of polygonal eyewalls (Schubert
 78 et al., 1999; Kuo et al., 1999; Rozoff et al., 2009; Kuo et al., 2016). While this frame-
 79 work can provide substantial insight, it has limitations in investigating eyewall dynam-
 80 ics as moist convective processes are very important to PV generation and the intensi-
 81 fication process. Diabatic heating can be introduced as a proxy via a mass-sink in shallow-
 82 water models (Hendricks et al., 2012, 2014) or simulated directly in 3-D full physics mod-
 83 els (Wu et al., 2016), but simulations may not represent the real-world physical mech-
 84 anisms correctly. Utilizing observational datasets is critical to validate theory and nu-
 85 matical simulations and improve our understanding of polygonal eyewalls in TCs and
 86 the relation to the intensity change. Prior studies have been limited in their ability to
 87 examine the dynamics of VRWs and polygonal eyewalls. Multi-Doppler airborne radar
 88 analyses (Reasor et al., 2000) can retrieve the full wind field, but have temporal sam-
 89 pling and aliasing limitations (Cha, 2018). Studies analyzing the shape of the eye in re-
 90 flectivity (Itano & Hosoya, 2013) or using reflectivity as a proxy for PV (Corbosiero et
 91 al., 2006) have limitations due to the fact that the reflectivity may not be fully coupled
 92 with the winds or PV (Moon & Nolan, 2015).

93 Analyses of Hurricane Michael (2018) presented herein demonstrate the first ob-
 94 servation of high-order VRW propagation using tangential wind asymmetries as a proxy
 95 for the PV signal. The results show that the propagation speeds of the waves are con-
 96 sistent with linear wave theory on a vortex and help to provide new insight into phys-
 97 ical mechanisms contributing to TC rapid intensification. Section 2 describes the observ-
 98 ing platform, quality control processes for the observations and analysis methodology.
 99 Section 3 introduces Michael's evolution with reflectivity, axisymmetric and asymmet-
 100 ric tangential winds retrieved by the GVTM technique, the operational radar temporal
 101 sampling limitations with high-wavenumbers propagation, and discusses the physical mech-
 102 anisms contributing to Michael's inner core variability. Conclusions and future work will
 103 be presented in section 4.

104 2 Data and Methods

105 Hurricane Michael was within range of ground-based radar surveillance during its
 106 approach to the Florida panhandle and brought in devastating winds and storm surge
 107 to the coastal area near Mexico beach and Tyndall Air Force Base (AFB). Figure 1 shows

108 the track, intensity, environmental vertical wind shear (VWS) direction, and reflectiv-
109 ity evolution at 3 km. Michael intensified nearly continuously from genesis to landfall,
110 and experienced two RI periods during its life cycle. The second RI started on 9 Octo-
111 ber and ended when the storm reached Category 5 intensity (140 kt) at the time of land-
112 fall around 1730 UTC. After the landfall, Michael underwent a rapid weakening and ex-
113 tratropical transition as the TC moved into North Carolina. The analysis period for this
114 study is from 1000 to 1930 UTC 10 October when the hurricane was within the coastal
115 radar detection range. The deep layer 200-850 hPa VWS magnitude was about 5 m s^{-1}
116 and the VWS direction transitioned from the southeast to the north-northeast during
117 the analysis period.

118 Figure 1a shows the TC tracks derived from three different methods: best track,
119 GVTD-simplex and dynamic aircraft location. The best track centers are surface-based
120 estimates from the National Hurricane Center (NHC) that consider satellite, ground-based
121 radars and in-situ measurements every 6 hours. The dynamic aircraft centers from Hur-
122 ricane Research Division (HRD) are derived from the NOAA P-3 (hereafter as P3) in-
123 situ measurements of wind and geopotential height at 700 hPa (Willoughby & Chelmow,
124 1982). The GVTD objective centers are obtained from the radar data at 3 km altitude
125 using a simplex method to obtain a set of possible circulation centers (W.-C. Lee et al.,
126 1999; W.-C. Lee & Marks, 2000) that are selected by an objective algorithm (Bell & Lee,
127 2012) to smooth the track and reduce the center uncertainty. The tracks derived from
128 the three different methods have similar trends in the earlier period, while the dynamic
129 centers show a trochoidal motion between 1200 UTC through 1400 UTC. Two hours be-
130 fore landfall the three tracks started to diverge, likely due to the difference in height of
131 the estimates and the impact of surface friction and VWS. In this study, we use the com-
132 bination of GVTD objective centers from 1000 to 1530 UTC and dynamic centers from
133 1530 to 1930 UTC for the analysis because the GVTD-simplex algorithm cannot find
134 the center accurately when the storm is close to the radar.

135 Data from the operational Weather Surveillance Doppler (WSR-88D) radar in Eglin
136 AFB, Florida (KEVX) were analyzed from 1000 to 1930 UTC 10 October. The radar
137 sweep files were processed with Lidar Radar Open Software Environment (LROSE) soft-
138 ware (Bell, 2019), and the National Center for Atmospheric Research (NCAR) SoloII soft-
139 ware (Bell et al., 2013) to correct Doppler velocity aliasing and remove the non-meteorological
140 echoes. The edited sweep files were then gridded using interpolation of the fields from

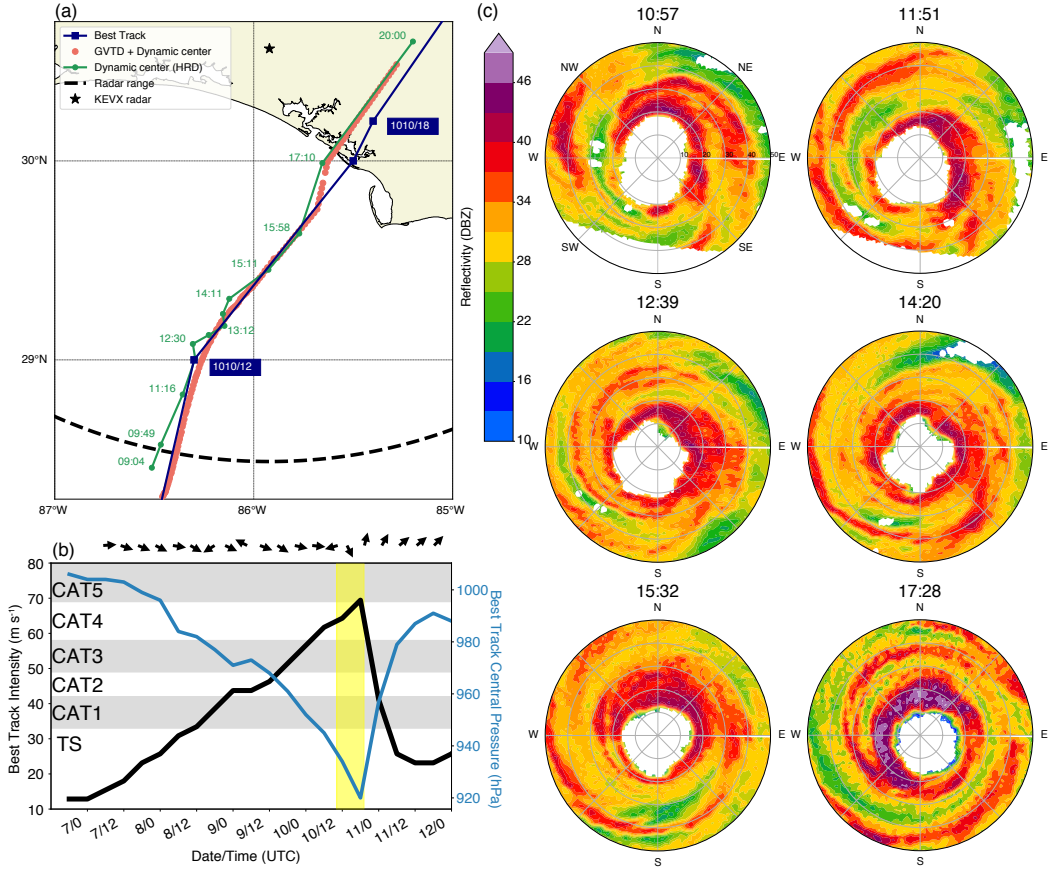


Figure 1. (a) Three tracks of Hurricane Michael on 10 October 2018 derived from best track from NHC (blue), GVTD objective centers (red), and dynamic centers (green) from NOAA HRD. (b) NHC best track wind intensity (black) and minimum central pressure (purple). The black arrow on the top row is the vertical wind shear direction (black) from the Statistical Hurricane Intensity Prediction Scheme (SHIPS) database (DeMaria et al., 2005). Yellow bar indicates the analysis period. (c) KEVX radar reflectivity scans at 1057, 1151, 1239, 1420, 1532, and 1728 UTC. The sequence of figures is from left to right and from top to bottom.

plan position indicators (elevation angle, Y, Z) to constant-altitude plan position indicators in Cartesian coordinate (X, Y, Z). The gridded data was further analyzed by the Vortex Objective Radar Tracking and Circulation (VORTRAC) software and the GVTD technique was used to retrieve the kinematic structure (Jou et al., 2008; Cha, 2018). The GVTD algorithm can retrieve the axisymmetric and asymmetric components of tangential winds and axisymmetric radial wind. More details can be found in Cha (2018).

147 In addition to the ground-based radar data, the P3 aircraft flew a reconnaissance
 148 mission from 0800 UTC to 1400 UTC 10 October and collected high-resolution airborne
 149 Doppler radar data. The flight pass from 1100 to 1130 UTC 10 October is analyzed in
 150 detail for this study to examine the 3-D kinematic structure from dual-Doppler synthesis
 151 using the SAMURAI variational analysis technique (Bell et al., 2012).

152 **3 Results**

153 Figure 1c shows a sequence of reflectivity images on October 10 that indicate in-
 154 tensification was accompanied by evolving reflectivity asymmetry. Michael's eyewall ex-
 155 hibited many noncircular shapes including ellipses, triangles, squares and hexagonal, which
 156 transitioned from low-high-low wavenumbers and then axisymmetrized. Most of the high-
 157 order features were short-lived, with the exception of an elliptical eyewall was traceable
 158 for an hour (1030 to 1130 UTC) with reflectivity maximized near the ends of the ma-
 159 jor ellipse axis at 1057 UTC. An hour later, the elliptical eyewall evolved into a trian-
 160 gle shape with reflectivity maximized on the eastern side. The asymmetries continued
 161 rotating cyclonically along the eyewall, and became dominated by wavenumber-1 asym-
 162 metry associated with spiral bands circulating around the eye at 1239 UTC. Michael's
 163 eyewall transitioned to a square shape at 1420 UTC, a quasi-triangular shape at 1532
 164 UTC, and eventually axisymmetrized to a near circular shape. After Michael made land-
 165 fall at 1730 UTC, the reflectivity decreased in the southeast eyewall, while the north-
 166 western quadrant had some of the highest reflectivity values seen during the analysis pe-
 167 riod exceeding 45 dBZ, suggesting an increasing impact of surface friction and shear.

168 Figure 2 shows a time-radius diagram of retrieved wind and derived dynamical quan-
 169 tities. The wavenumber-0 (axisymmetric) tangential wind (Fig. 2a) steadily intensified
 170 until landfall with a broadening outer wind field out to 100 km radius. The mean tan-
 171 gential wind reached its maximum intensity ($\sim 65 \text{ m s}^{-1}$) around 1700 UTC then de-
 172 cayed due to land interaction and increasing shear throughout the rest of analysis pe-
 173 riod. Figures 2b and c show the evolution of eyewall axisymmetric vorticity and its ra-
 174 dial gradient out to 30 km radius. The corresponding amplitude of the wavenumber 0
 175 – 4 tangential wind components is shown in Fig. 2d, with the black line denoting the peak
 176 axisymmetric wind and bars denoting the asymmetric components. Due to the differ-
 177 ence in magnitude of the asymmetric components, the normalized amplitude is shown
 178 in Figs. 2e-h using the time-mean value of each wavenumber within the eyewall region

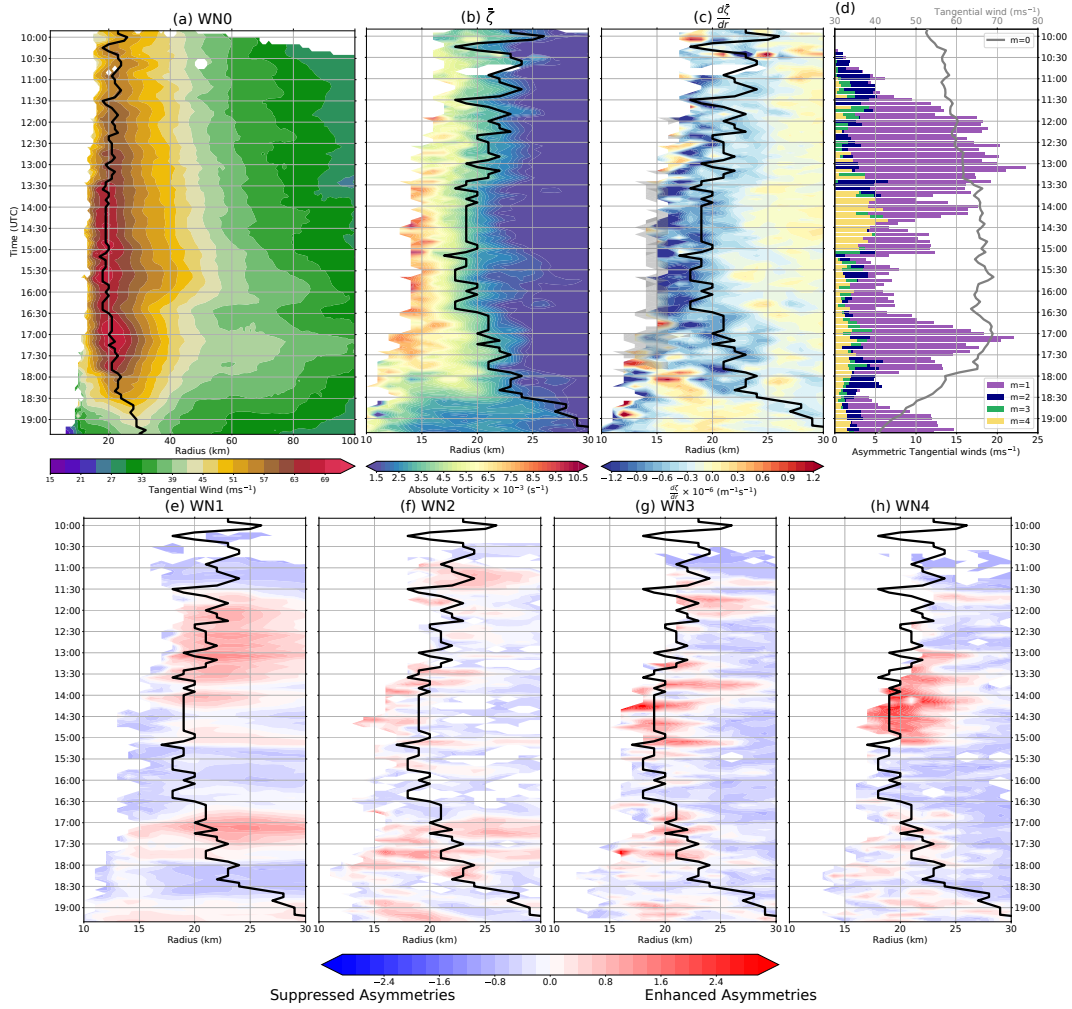


Figure 2. Single Doppler radar data collected in Hurricane Michael between 10 and 1930 UTC 10 October 2018. Time-Raidus diagram of the (a) wavenumber-0 tangential wind (b) mean vorticity (c) mean radial vorticity gradient at $z = 3$ km. (d) Time series of maximum amplitude of wavenumbers from $m = 0 - 4$. Time-Raidus diagram of the $m = 1 - 4$ normalized tangential wind at $z = 3$ km for (e) - (h). The black line in (a) - (c) and (e) - (h) indicates the radius of maximum wavenumber-0 tangential wind.

as a normalization factor, such that $V_{norm,m} = (V_m - \bar{V}_m)/\bar{V}_m$, where V_m is the instantaneous amplitude for each wavenumber m and \bar{V}_m is the time-mean value of the amplitude averaged between RMW - 5 to RMW + 5. The normalization more clearly visualizes the relative changes in asymmetric tangential wind with warm colors denoting enhanced asymmetries and cool colors denoting reduced asymmetries.

184 Early in the analysis period around 1030 UTC, the elliptical eyewall seen in the
185 radar reflectivity (Fig. 1c) is also evident in the retrieved wavenumber-2 tangential wind
186 component (Fig. 2f). By 1130 UTC, both wavenumbers-1 and 3 components strength-
187 ened (Figs. 2e and g). Between 1200 to 1330 UTC, the eyewall was dominated by a wavenumber-
188 1 asymmetry that continued to intensify up to $\approx 23 \text{ m s}^{-1}$. Enhanced wavenumber-1
189 asymmetry is mostly diagnosed as a result from the VWS impact, but the local VWS
190 magnitude from the P3 flight radar analysis was only 2.9 m s^{-1} , suggesting that VWS
191 was not the cause of the increasing wavenumber-1 asymmetry. The GVTM analysis and
192 P3 in situ data suggests that wavenumber-1 asymmetries seemed more likely to be con-
193 nected to internal processes in the inner core due to the presence of a trochoidal oscil-
194 lation of the center at this time. Around 1300 UTC as the wavenumber-1 was near its
195 maximum amplitude, the higher-order asymmetries were suppressed and the mean vor-
196 ticity in the inner core decreased slightly. The analysis shows an appearance of a sign
197 reversal of the mean radial vorticity gradient inside the RMW, suggesting the onset of
198 dynamic instability.

199 One hypothesis for the wavenumber-1 asymmetry evolution as an algebraic insta-
200 bility was proposed by Smith and Rosenbluth (1990) and Nolan and Montgomery (2000).
201 The algebraic instability is different from the barotropic instability, and the initial con-
202 dition requires to have initial perturbation vorticity inside of the angular velocity max-
203 imum for the growth to occur. Enhanced eye-eyewall mixing by the prior wavenumber-
204 2 and 3 asymmetries may have provided that initial perturbation vorticity, but due to
205 the lack of scatterers in the eye we cannot verify whether that was the case. Nolan and
206 Montgomery (2000) showed that the presence of a wavenumber-1 algebraic instability
207 causes the TC center to have trochoidal motion with respect to the time-averaged mo-
208 tion vector. The dynamic centers derived from aircraft in situ winds (Fig. 1a) show a
209 trochoidal motion from 1223 to 1430 UTC that is consistent with the theoretical growth
210 of this instability.

211 Between 1330 to 1500 UTC, high wavenumbers 3-4 grew in amplitude as the wavenumber-
212 1 amplitude decreased. The RMW contracted during this period and the mean vortic-
213 ity in the inner core strengthened to greater than $6 \times 10^{-3} \text{ s}^{-1}$. At 1530 UTC the eye-
214 wall reflectivity pattern was triangular (Fig. 1c), consistent with the retrieved wavenumber-
215 3 wind asymmetry at this time. Subsequently, Michael gradually axisymmetrized as the
216 mean vortex intensified and the asymmetric components of tangential wind weakened

217 by 1630 UTC. The RMW then began to expand and the magnitude of asymmetries in-
218 creased again as the hurricane continued the northeastward trajectory and started to be
219 impacted by the land interaction. Michael made landfall at 1730 UTC as the environ-
220 mental VWS concurrently intensified and the hurricane intensity weakened significantly.

221 The analysis of Michael's inner core evolution suggests that the asymmetric VRWs
222 dynamics played an important role in modulating the structure and intensity changes.
223 As described in the introduction, previous observational analyses have yet to document
224 the high-wavenumber kinematic structure propagation due to lack of both high spatial
225 and temporal resolution data. Here we use the GVTD retrieved asymmetric tangential
226 winds as a proxy for vorticity and utilize the high temporal resolution to estimate the
227 azimuthal propagation speed. Figure 3a shows an azimuth-time diagram of wavenumber-
228 2 wind near the RMW during the period with a rotating elliptical eyewall. There is a
229 clear cyclonic propagation of the wavenumber-2 amplitude during this time. Concurrent
230 with this propagation, the mean vorticity structure derived from both P3 dual-Doppler
231 and single Doppler radar analysis (Fig. 3b) shows a steep vorticity gradient at the in-
232 ner edge of the eyewall that would support VRW propagation. There is a good agree-
233 ment in the retrieved axisymmetric vorticity across all radii, providing confidence in the
234 radar analysis for investigating the vortex dynamics.

235 The enhanced sensitivity and pseudo dual-Doppler scanning strategy of the P3 al-
236 low for a retrieval of the full axisymmetric kinematic structure at the time of the aircraft
237 penetration. Figure 3c shows the radius-height structure of vorticity, tangential wind,
238 and secondary circulation. A local maximum of vorticity exceeding $9 \times 10^{-3} \text{ s}^{-1}$ is ev-
239 ident in the low-levels, with a tower of positive vorticity extending to the upper tropo-
240 sphere. A updraft maximum in the upper-levels suggests an ongoing development of the
241 vorticity tower in the vertical. Due to the enhanced sensitivity of the P3 radar in the
242 storm, a reversal in the vorticity gradient at the inner edge of the eyewall is captured
243 by the dual-Doppler analysis at upper levels, and can be inferred at low-levels (Fig. 3d).
244 The couplet of positive and negative radial gradient of vorticity satisfies the Rayleigh
245 condition for barotropic instability that could support the exponential growth of higher
246 order asymmetries. The tightly packed angular momentum surfaces in Fig. 3d are nearly
247 upright in low-levels and slant outward in approximate congruence with the secondary
248 circulation at upper-levels.

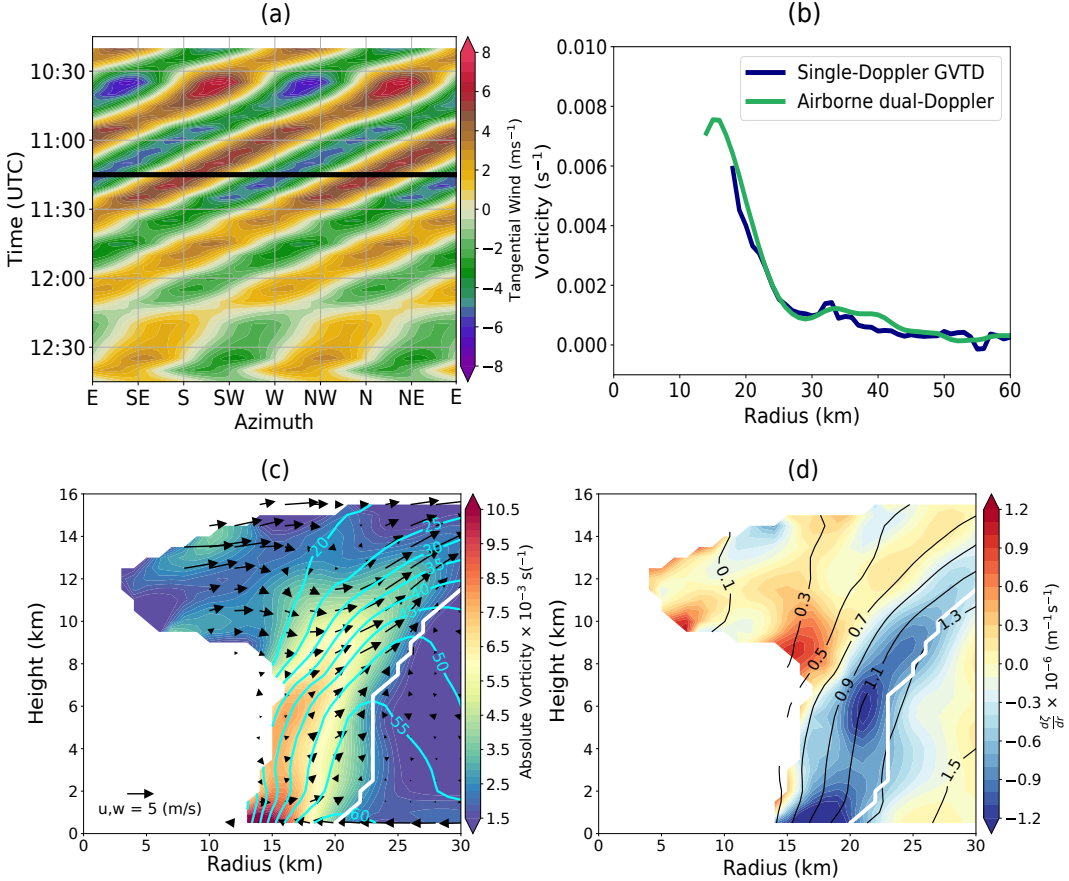


Figure 3. (a) Time-azimuth diagram of the wavenumber-2 tangential wind at $z = 3$ km averaged from $r = \text{RMW} - 3$ to $r = \text{RMW} + 3$. (b) The radial profile of axisymmetric absolute vorticity derived from the P-3 dual-Doppler analysis (green) and the single-Doppler GVD retrieval (blue) at $z = 3$ km. Radius-height diagram of (c) azimuthal mean storm-relative absolute vorticity (shading), secondary circulation (vector), tangential wind (cyan contour), and radius of maximum wind (white contour), (d) azimuthal mean storm-relative radial gradient of absolute vorticity (shading) and angular momentum surfaces (black contour) from the P-3 dual-Doppler analysis.

The elliptical and triangle eyewall patterns are hypothesized to be the result of combined barotropic/baroclinic instability. The presence of the hollow vorticity tower during that period (Fig. 3) suggests that wavenumber 2 and 3 modes could grow through via barotropic/baroclinic instability (Terwey & Montgomery, 2002) and result in vorticity mixing between the eye and eyewall. This vorticity mixing can transport the perturbation vorticity into the core, and can lead to weakening of the symmetric vortex. In Hurricane Michael however, sustained deep convection and vortex stretching were evidently

able to maintain and intensify the symmetric vorticity tower despite the growth of asymmetric perturbations.

A power spectrum analysis in the frequency domain of the tangential wind and reflectivity were performed in order to calculate the propagation speed of the asymmetries quantitatively (Figs 4 a and b). Linear trends in the time series were removed prior to spectral analysis to minimize the impact from spectral leakage to other wave numbers. The asymmetric tangential winds have clearly separated spectral peaks that correspond to different azimuthal propagation speeds. The asymmetric reflectivity spectra have distinguishable peaks for the propagation signals for low wavenumbers ($m = 1$ and 2) , whereas the high-wavenumber signals ($m > 2$) are noisier and have multiple peaks of signal which is hard to recognize the propagation velocity.

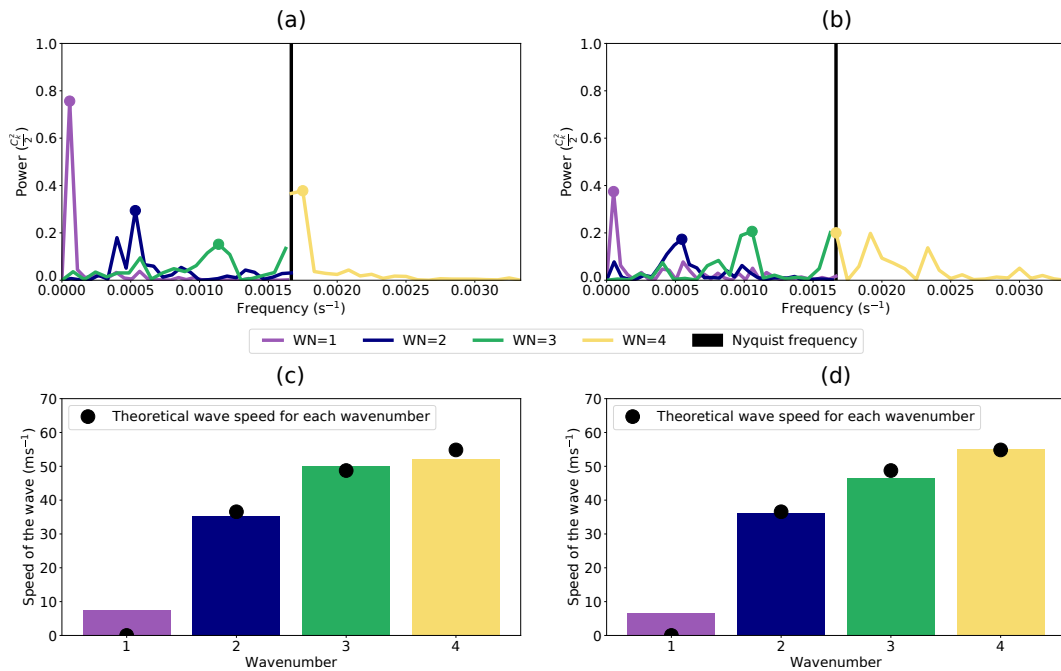


Figure 4. Spectral time decomposition of $m = 1 - 4$ (a) tangential wind components (b) reflectivity components. The derived propagation speeds of each (c) tangential wavenumber and (d) reflectivity wavenumber and the theoretical VRWs propagation speed from the linear wave theory.

Figures 4 c and d display the theoretical speed calculated from equation S1 and the observed speed. The strongest power of each wavenumber is selected as the observed VRW propagation velocity. In the supporting information we provide the derivation of

azimuthal velocity of each wavenumber. The observed values are remarkably consistent with the linear wave theory, suggesting that the observed asymmetries are well-described by VRW theory. Moreover, the propagation speeds of asymmetric reflectivity signals are also consistent with the linear wave theory (Fig. 4 d) despite the broader power spectra. The observed asymmetric propagation of both wind and reflectivity provides further support for the theoretical framework of linear wave theory, suggesting that non-linear wave interaction may be of secondary importance in the propagation speed.

The similar propagation speed of tangential wind and reflectivity at the altitude of 3 km implies that the vorticity and divergence fields are coupled together in the low to mid-troposphere. Due to sampling limitations of the radar beam, it is unclear whether this coupling originates in the boundary layer or is only in the free troposphere. Kuo et al. (2016) used a nondivergent barotropic model for the free atmosphere and an asymmetric slab boundary layer underneath and found a tangential wind maximum at the minor axis of the elliptic vortex in the free atmosphere, whereas the wind maximum was closer to the major axis within the boundary layer. In a real, baroclinic vortex that decays with height, the theoretical wave speed for VRWs is height dependent such that a vertically coherent asymmetry that propagates at the same speed over some depth will deviate from the theory at different levels. While Michael's symmetric vorticity tower was quite strong through the depth of the troposphere (Fig. 3c), the mean flow still decayed with height suggesting barotropic theory cannot fully describe the evolution. The good correspondence between theoretical and observed wave speeds does indicate that barotropic theory is a reasonable approximation in this case.

Previous studies have shown that the vortex structure and the location of diabatic heating play important roles in the intensification of TCs (Schubert & Hack, 1982). Latent heat release is the leading order effect in PV generation in the TC inner-core and VRWs can transport the diabatically generated PV inward (Chen & Yau, 2001). In barotropic models, mixing associated with VRW activity leads to weakening of the symmetric vortex. The simultaneous amplification of symmetric vortex (Fig. 2b) and cycles of intensification and weakening of asymmetries (Fig. 3d) throughout the RI stage suggest that the asymmetries are not necessarily a negative impact on TC intensification, consistent with the recent study by J.-D. L. Lee and Wu (2018). Whether the vortex would have intensified even more rapidly in the absence of the asymmetries is unknown and remains to be explored with numerical modeling in future work.

303 **4 Conclusion**

304 The structure and evolution of Hurricane Michael were examined using single Doppler
305 radar observations, providing the first observational evidence of the evolving wind field
306 of a polygonal eyewall during rapid intensification (RI) to Category 5 intensity. Quan-
307 titative evidence of growing structures with low (1 - 4) azimuthal wavenumbers in the
308 tangential wind and reflectivity fields suggest the presence of rapidly-evolving vortex Rossby
309 waves (VRWs). A spectral time decomposition analysis of the retrieved winds indicates
310 that the propagation speeds of different VRWs are consistent with linear wave theory
311 on a symmetric radial vorticity gradient. The appearance and growth of the asymme-
312 tries is proposed to be the result of a combination of wavenumber-1 algebraic instabil-
313 ities and higher order barotropic/baroclinic instabilities. Aircraft center fixes document
314 a period of trochoidal motion with an enhanced wavenumber-1 asymmetry when all other
315 higher wavenumber asymmetries were suppressed. A period of higher-order VRW growth
316 followed as the mean radial vorticity gradient amplified and the hollow vortex tower con-
317 tracted, eventually becoming nearly symmetric prior to landfall. The simultaneous am-
318 plification of the symmetric vortex and cycles of growth and decay of asymmetries sug-
319 gest that they were closely coupled. After Michael made landfall, both wind intensity
320 and minimum pressure weakened significantly and the asymmetries increased due to land
321 friction and increasing vertical wind shear.

322 The results presented here highlight the value of coastal radar observations to in-
323 vestigate physical mechanisms of TC intensity and structure evolution with high tem-
324 poral and spatial resolution. Airborne dual-Doppler radar analysis supports the single
325 Doppler wind retrievals and documents the vertical structure of the growing vorticity
326 tower, indicating the necessary condition for barotropic/baroclinic instability. The evo-
327 lution of the vorticity gradient derived from the single Doppler analysis further presents
328 new insights on intensity and structure change, which will help to improve TC forecasts
329 in the future. In addition, both the reflectivity and tangential winds show evidence of
330 polygonal structure and propagate at a similar speed, indicating that the vorticity and
331 divergence fields are closely coupled together. The interaction between the asymmetric
332 vortex dynamics and diabatic generation of PV by the convection may play a salient role
333 in rapid intensification and is an important topic for future research.

334 **Acknowledgments**

335 This research was supported by National Science Foundation awards AGS-1701225 and
 336 OAC-1661663, and Office of Naval Research awards N000141613033 and N000142012069.

337 **References**

- 338 Bell, M. M. (2019). nsf-lrose/lrose-blaze: lrose-blaze-20190105.
 339 doi: 10.5281/zenodo.2532758
- 340 Bell, M. M., & Lee, W.-C. (2012). Objective tropical cyclone center tracking using
 341 single-Doppler radar. *Journal of Applied Meteorology and Climatology*, 51(5),
 342 878–896. doi: 10.1175/JAMC-D-11-0167.1
- 343 Bell, M. M., Lee, W.-C., Wolff, C. A., & Cai, H. (2013). A Solo-based automated
 344 quality control algorithm for airborne tail Doppler radar data. *J. Appl. Me-
 345 teor. Climatol.*, 52(11), 2509–2528. doi: 10.1175/JAMC-D-12-0283.1
- 346 Bell, M. M., & Montgomery, M. T. (2008). Observed structure, evolution,
 347 and potential intensity of Category 5 Hurricane Isabel (2003) from 12
 348 to 14 September. *Monthly Weather Review*, 136(6), 2023–2046. doi:
 349 10.1175/2007MWR1858.1
- 350 Bell, M. M., Montgomery, M. T., & Emanuel, K. A. (2012). Air-sea enthalpy
 351 and momentum exchange at major hurricane wind speeds observed during
 352 CBLAST. *Journal of the Atmospheric Sciences*, 69(11), 3197–3222. doi:
 353 10.1175/JAS-D-11-0276.1
- 354 Beven II, R. B., L. J., & Hagen, A. (2019). Hurricane Michael (2018). *National Hur-
 355 ricane Center Tropical Cyclone Report*, 86.
- 356 Cha, T.-Y. (2018). Eyewall replacement cycle of Hurricane Matthew (2016) observed
 357 by Doppler radars. *M. S. Thesis*, Colorado State University.
- 358 Chen, Y., & Yau, M. K. (2001). Spiral bands in a simulated hurricane. Part I:
 359 Vortex rossby wave verification. *Journal of the Atmospheric Sciences*, 58(15),
 360 2128–2145. doi: 10.1175/1520-0469(2001)058<2128:SBIASH>2.0.CO;2
- 361 Corbosiero, K. L., Molinari, J., Aiyyer, A. R., & Black, M. L. (2006). The struc-
 362 ture and evolution of Hurricane Elena (1985). Part II: Convective asymmetries
 363 and evidence for Vortex Rossby Waves. *Monthly Weather Review*, 134(11),
 364 3073–3091. doi: 10.1175/MWR3250.1

- 365 DeMaria, M., Mainelli, M., Shay, L. K., Knaff, J. A., & Kaplan, J. (2005). Further
366 improvements to the statistical hurricane intensity prediction scheme (SHIPS).
367 *Weather and Forecasting*, 20(4), 531–543. doi: 10.1175/WAF862.1
- 368 Hendricks, E. A., McNoldy, B. D., & Schubert, W. H. (2012). Observed inner-core
369 structural variability in Hurricane Dolly (2008). *Monthly Weather Review*,
370 140(12), 4066–4077. doi: 10.1175/MWR-D-12-00018.1
- 371 Hendricks, E. A., Peng, M. S., Fu, B., & Li, T. (2010). Quantifying environmental
372 control on tropical cyclone intensity change. *Monthly Weather Review*, 138(8),
373 3243–3271. doi: 10.1175/2010MWR3185.1
- 374 Hendricks, E. A., Schubert, W. H., Chen, Y.-H., Kuo, H.-C., & Peng, M. S. (2014).
375 Hurricane eyewall evolution in a forced shallow-water model. *Journal of the*
376 *Atmospheric Sciences*, 71(5), 1623–1643. doi: 10.1175/JAS-D-13-0303.1
- 377 Itano, T., & Hosoya, M. (2013). Spectral analyses of the polygonal eye of Typhoon
378 Sinlaku. *Monthly Weather Review*, 141(3), 987–996. doi: 10.1175/MWR-D-12
379 -00122.1
- 380 Jou, B. J.-D., Lee, W.-C., Liu, S.-P., & Kao, Y.-C. (2008). Generalized VTD
381 retrieval of atmospheric vortex kinematic structure. Part I: Formulation
382 and error analysis. *Monthly Weather Review*, 136(3), 995–1012. doi:
383 10.1175/2007MWR2116.1
- 384 Kossin, J. P., & Eastin, M. D. (2001). Two distinct regimes in the kinematic and
385 thermodynamic structure of the hurricane eye and eyewall. *Journal of the At-*
386 *mospheric Sciences*, 58(9), 1079–1090. doi: 10.1175/1520-0469(2001)058<1079:
387 TDRITK>2.0.CO;2
- 388 Kuo, H.-C., Cheng, W.-Y., Yang, Y.-T., Hendricks, E. A., & Peng, M. S. (2016).
389 Deep convection in elliptical and polygonal eyewalls of tropical cyclones.
390 *Journal of Geophysical Research: Atmospheres*, 121(24). doi: 10.1002/
391 2016JD025317
- 392 Kuo, H.-C., Williams, R., & Chen, J.-H. (1999). A possible mechanism for the eye
393 rotation of Typhoon Herb. *Journal of the Atmospheric Sciences*, 56(11), 1659–
394 1673. doi: 10.1175/1520-0469(1999)056<1659:APMFTE>2.0.CO;2
- 395 Lee, J.-D. L., & Wu, C.-C. (2018). The role of polygonal eyewalls in rapid intensi-
396 fication of typhoon Megi (2010). *Journal of the Atmospheric Sciences*, 75(12),
397 4175–4199. doi: 10.1175/JAS-D-18-0100.1

- 398 Lee, W.-C., & Bell, M. M. (2007). Rapid intensification, eyewall contraction, and
399 breakdown of Hurricane Charley (2004) near landfall. *Geophysical Research*
400 *Letters*, 34(2). doi: 10.1029/2006GL027889
- 401 Lee, W.-C., Jou, B. J.-D., Chang, P.-L., & Deng, S.-M. (1999). Tropical cy-
402 clone kinematic structure retrieved from single-Doppler radar observa-
403 tions. Part I: Interpretation of Doppler velocity patterns and the GB-
404 VTD technique. *Monthly Weather Review*, 127(10), 2419–2439. doi:
405 10.1175/1520-0493(1999)127<2419:TCKSRF>2.0.CO;2
- 406 Lee, W.-C., & Marks, F. D. (2000). Tropical cyclone kinematic structure retrieved
407 from single-Doppler radar observations. Part II: The GBVTD-simplex cen-
408 ter finding algorithm. *Monthly Weather Review*, 128(6), 1925–1936. doi:
409 10.1175/1520-0493(2000)128<1925:TCKSRF>2.0.CO;2
- 410 Martinez, J., Bell, M. M., Rogers, R. F., & Doyle, J. D. (2019). Axisymmetric po-
411 tential vorticity evolution of Hurricane Patricia (2015). *Journal of the Atmo-*
412 *spheric Sciences*, 76(7), 2043–2063. doi: 10.1175/JAS-D-18-0373.1
- 413 Martinez, J., Bell, M. M., Vigh, J. L., & Rogers, R. F. (2017). Examining
414 tropical cyclone structure and intensification with the FLIGHT+ dataset
415 from 1999 to 2012. *Monthly Weather Review*, 145(11), 4401–4421. doi:
416 10.1175/MWR-D-17-0011.1
- 417 Menelaou, K., & Yau, M. (2014). On the role of asymmetric convective bursts to
418 the problem of hurricane intensification: Radiation of Vortex Rossby waves
419 and wave-mean flow interactions. *Journal of the Atmospheric Sciences*, 71(6),
420 2057–2077. doi: 10.1175/JAS-D-13-0343.1
- 421 Montgomery, M. T., & Shapiro, L. J. (1995). Generalized charney–stern and fjortoft
422 theorems for rapidly rotating vortices. *Journal of the Atmospheric Sciences*,
423 52(10), 1829–1833. doi: 10.1175/1520-0469(1995)052<1829:GCAFTF>2.0.CO;
424 2
- 425 Moon, Y., & Nolan, D. S. (2015). Spiral rainbands in a numerical simulation of Hur-
426 rricane Bill (2009). Part II: Propagation of inner rainbands. *Journal of the At-*
427 *mospheric Sciences*, 72(1), 191–215. doi: 10.1175/JAS-D-14-0056.1
- 428 Muramatsu, T. (1986). The structure of polygonal eye of a typhoon. *Journal of the*
429 *Meteorological Society of Japan. Ser. II*, 64(6), 913–921. doi: 10.2151/jmsj1965
430 .64.6_913

- 431 Nolan, D. S., & Montgomery, M. T. (2000). The algebraic growth of wavenumber
432 one disturbances in hurricane-like vortices. *Journal of the Atmospheric Sciences*, 57(21), 3514–3538. doi: 10.1175/1520-0469(2000)057<3514:TAGOWO>2
433 .0.CO;2
- 435 Reasor, P. D., Montgomery, M. T., Marks, F. D., & Gamache, J. F. (2000). Low-
436 wavenumber structure and evolution of the hurricane inner core observed by
437 airborne dual-Doppler radar. *Monthly Weather Review*, 128(6), 1653–1680.
438 doi: 10.1175/1520-0493(2000)128<1653:LWSAEO>2.0.CO;2
- 439 Rozoff, C. M., Kossin, J. P., Schubert, W. H., & Mulero, P. J. (2009). Internal
440 control of hurricane intensity variability: The dual nature of potential vor-
441 ticity mixing. *Journal of the Atmospheric Sciences*, 66(1), 133–147. doi:
442 10.1175/2008JAS2717.1
- 443 Schubert, W. H., & Hack, J. J. (1982). Inertial stability and tropical cyclone devel-
444 opment. *Journal of the Atmospheric Sciences*, 39(8), 1687–1697. doi: 10.1175/
445 1520-0469(1982)039<1687:ISATCD>2.0.CO;2
- 446 Schubert, W. H., Montgomery, M. T., Taft, R. K., Guinn, T. A., Fulton, S. R.,
447 Kossin, J. P., & Edwards, J. P. (1999). Polygonal eyewalls, asymmetric eye
448 contraction, and potential vorticity mixing in hurricanes. *Journal of the At-
449 mospheric Sciences*, 56(9), 1197–1223. doi: 10.1175/1520-0469(1999)056<1197:
450 PEAECA>2.0.CO;2
- 451 Shimada, U., Sawada, M., & Yamada, H. (2018). Doppler radar analysis of the rapid
452 intensification of Typhoon Goni (2015) after Eyewall Replacement. *Journal of*
453 *the Atmospheric Sciences*, 75(1), 143–162. doi: 10.1175/JAS-D-17-0042.1
- 454 Smith, R. A., & Rosenbluth, M. N. (1990, Feb). Algebraic instability of hollow elec-
455 tron columns and cylindrical vortices. *Phys. Rev. Lett.*, 64, 649–652. doi: 10
456 .1103/PhysRevLett.64.649
- 457 Terwey, W. D., & Montgomery, M. T. (2002). Wavenumber-2 and wavenumber-m
458 Vortex Rossby Wave instabilities in a generalized three-region model. *Journal*
459 *of the Atmospheric Sciences*, 59(16), 2421–2427. doi: 10.1175/1520-0469(2002)
460 059<2421:WAWMVR>2.0.CO;2
- 461 Willoughby, H. E., & Chelmow, M. B. (1982). Objective determination of hur-
462 rricane tracks from aircraft observations. *Monthly Weather Review*, 110(9),
463 1298–1305. doi: 10.1175/1520-0493(1982)110<1298:ODOHTF>2.0.CO;2

- 464 Wu, C.-C., Wu, S.-N., Wei, H.-H., & Abarca, S. F. (2016). The role of convective
465 heating in tropical cyclone eyewall ring evolution. *Journal of the Atmospheric*
466 *Sciences*, 73(1), 319-330. doi: 10.1175/JAS-D-15-0085.1